Anisotropic Colloidal Interactions & Assembly in AC Electric Fields

Journal:	*Soft Matter*
Manuscript ID	SM-ART-08-2021-001227.R1
Article Type:	Paper
Date Submitted by the Author:	17-Sep-2021
Complete List of Authors:	Hendley, Rachel; Johns Hopkins University Torres-Diaz, Isaac; Johns Hopkins University Bevan, Michael; Johns Hopkins University

SCHOLARONE™
Manuscripts

Anisotropic Colloidal Interactions & Assembly in AC Electric Fields

Rachel S. Hendley, Isaac Torres-Díaz[†] & Michael A. Bevan∗
Chemical & Biomolecular Engr., Johns Hopkins Univ., Baltimore, MD 21218

Abstract

We match experimental and simulated configurations of anisotropic epoxy colloidal particles in high frequency AC electric fields by identifying analytical potentials for dipole-field and dipole-dipole interactions. We report an inverse Monte Carlo simulation algorithm to determine optimal fits of analytical potentials by matching simulated and experimental distribution functions for non-uniform liquid, liquid crystal, and crystal microstructures in varying amplitude electric fields. Two potentials that include accurate particle volume and dimensions along with a concentration dependent prefactor quantitatively capture experimental observations. At low concentrations, an effective ellipsoidal point dipole potential works well, whereas a novel stretched point dipole potential is found to be suitable at all concentrations, field amplitudes, and degrees of ordering. The simplicity, accuracy, and adjustability of the stretched point dipole potential suggest it can be applied to model field mediated microstructures and assembly of systematically varying anisotropic particle shapes.

Introduction

Assembly of anisotropic colloidal particles on surfaces could enable novel multifunctional material coatings for use in diverse applications.[1] Practically, anisotropic colloidal building blocks can create microstructured materials with directional properties (e.g., optical, mechanical, wetting, adhesion, thermal, etc.) that are not attainable with spherical particles. Many natural biological materials from plants and animals have such multifunctional directional microstructures, but cannot currently be fabricated in synthetic materials systems in a reliable scalable manner.[2] In many cases, anisotropic colloidal building blocks could be assembled into target microstructures with the key features to enable multifunctional surface structures. External fields have been used to assemble colloidal building blocks primarily into liquid crystalline configurations including representative examples involving shear,[3] electric,[4] magnetic,[5] acoustic,[6] and other fields.[7] To understand and design how different structures of anisotropic colloids assemble in external fields, it is useful to know the connections between field-mediated potentials and equilibrium microstructures in liquid, liquid crystalline, and crystalline phases.

AC electric field mediated assembly of anisotropic colloids is perhaps the most attractive field type for a number of reasons. Electric fields are relatively easy to design, shape, and control across a range of length scales, which can lead to scalable technologies (*e.g.*, liquid crystal displays, Xerography). Because AC electric fields can be used to induce dipolar interactions in a broad range of materials, electric field mediated assembly does not require very specific material properties (e.g., magnetic, optical). Tuning AC electric field shape, frequency, and amplitude can be used to control position and orientations of single particles and particle ensembles,[8-10] which offers significant control authority over assembly processes. A large number of experiments have

demonstrated assembly of different microstructures from particle shapes including dumbbells,[11, 12] cylinders,[13, 14] capsules,[15, 16] and patchy particles.[17-19] In addition, tuning field shape, frequency, and amplitude has been shown produce controllable microstructures using spherical particles,[20-22] and to a lesser extent for anisotropic particles.[15, 23] As such, a number of significant scientific questions and engineering challenges are directly related to measuring and modeling equilibrium phase behavior and dipolar interactions for anisotropic colloidal particles in AC electric fields.

Prior studies have modelled potentials of anisotropic particles in AC electric fields with connections to measured microstructures. Several studies have simulated configurations with qualitative similarities to experimentally observed states simply by separating opposite sign point charges at either end of ellipsoids to produce dipoles. This approach has been used to successfully generate configurations similar to colloidal ellipsoids assembled into microtubules[24] and fibers[25] as well as phase diagrams qualitatively consistent with microscopy images of cylindrical colloidal particles.[23] Another approach has been to discretize particles into polarizable sub-units,[26] which has captured the projected orientation distribution of three dimensional nematic phases of cylindrical colloids.[27] Finally, the electric potential has been computed around ellipsoidal colloidal particles[28] as part of understanding their relative positions within chain configurations in AC electric fields.[29] However, dipole-field and dipole-dipole theoretical potentials have not been directly compared with experimental observables using forms that are easily generalizable for
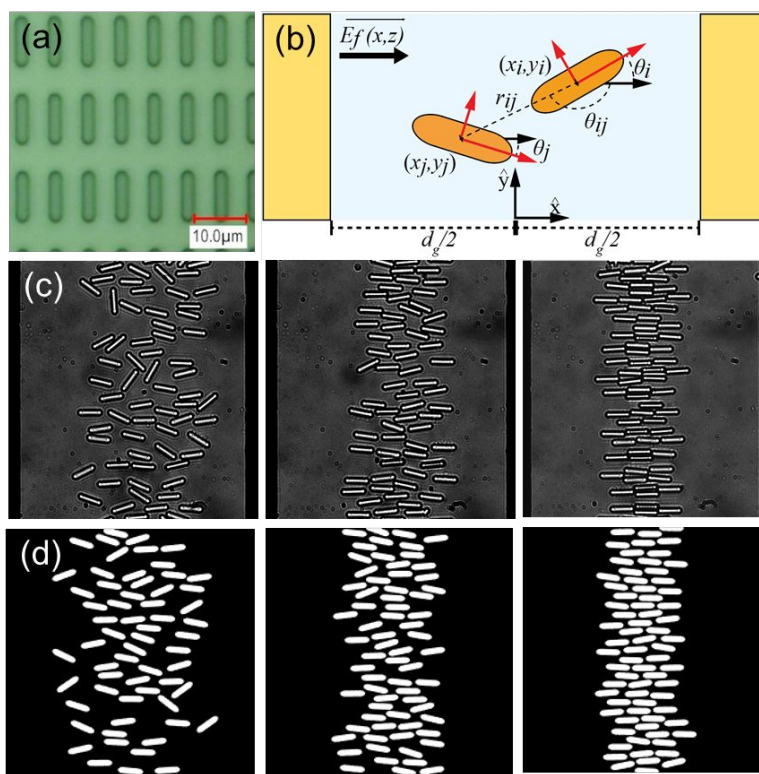
Fig. 1. Overview of anisotropic particle fabrication, and coordinate system for interaction potentials, AC electric field mediated assembly, (a) Microfabricated photolithographic SU8 colloidal particles on wafer before release into solution. (b) Schematic of coordinate system used in theoretical interaction potentials showing parallel electrodes, electric field, and two dimensional laboratory and particle coordinates. (c) Optical microscopy images of AC electric field mediated assembly between electrodes within a thin monolayer above the microscopy slide surface at 4.1, 10, and 42 V/mm. (d) Renderings from Monte Carlo simulation using the stretched point dipole model at the same field conditions.

different particle shapes, material properties, field conditions (*e.g.*, frequency, amplitude, non-uniformity), and microstructures (*e.g.*, liquid, liquid crystal, crystal phases).

Here, we report an inverse scheme to determine interaction potentials for anisotropic colloidal particles in AC electric fields based on optical microscopy measurements. Microscopy experiments are performed on microfabricated epoxy tri-axial particles sedimented into quasi-two-dimensional configurations on a microscope slide, where they are confined between electrodes via induced dipolar interactions with non-uniform AC electric fields (**Fig. 1**). Single particle dipole-field interaction potentials were previously measured and modelled for similar anisotropic particles, which demonstrated position and orientation dependence vs. field amplitude and frequency[9, 10] and reduce to previously measured potentials for spherical colloids.[21, 22, 30] By conducting experiments at high AC field frequencies (5MHz), particles align with the field and concentrate at the electric field minimum at the electrode center. We vary electric field amplitude to simultaneously control the dipole-field and dipole-dipole potentials. Next, we develop an inverse Monte Carlo simulation method to determine dipole-dipole potentials by matching simulated and experimental pair distribution functions, orientation distributions, and concentration profiles within non-uniform field. Several analytical dipole-dipole potentials are investigated to determine the best model for capturing anisotropic colloidal phase behavior in AC electric fields.

Theory

Net Interaction Potential

The net potential energy of a colloidal particle in an AC electric field is given by,

$$u_i\left(\mathbf{X}_i,\mathbf{\Theta}_i,\mathbf{X}_j,\mathbf{\Theta}_j\right) = u_i^{grav}\left(\mathbf{X}_i\right) + u_i^{pw}\left(\mathbf{X}_i,\mathbf{\Theta}_i\right) + u_i^{df}\left(\mathbf{X}_i,\mathbf{\Theta}_i\right) + \sum_{j=1,i\neq j}^{N}\left(u_{ij}^{pp}\left(\mathbf{X}_i,\mathbf{\Theta}_i,\mathbf{X}_j,\mathbf{\Theta}_j\right)\right) \quad (1)$$

where $\mathbf{X}_i = (x,y,z)$ and $\mathbf{\Theta}_i = (\theta,\varphi,\psi)$ are the Cartesian position and Euler angles of particle *i*. The net potential includes particle *i* interacting with a gravitational field (u^{grav}), a substrate surface (u^{pw}), an applied AC electric field (u^{df}), and all other *j* particles (u^{pp}). For anisotropic particles where the potential energy associated with elevating one end relative to the other is $>5kT$, the long axis is primarily parallel to the substrate.[31] By considering the balance of electrostatic and gravitational interactions normal to the substrate of a cylinder, the particle's most probable elevation, h_m, is estimated as,[31]

$$h_m = \kappa^{-1}\ln\left[\frac{\left(\kappa^3 bc/4\pi\right)^{0.5} B^{pw}}{bc\left(\rho_m - \rho_p\right)g}\right], \quad B^{pw} = 64\varepsilon_m\left(\frac{kT}{e}\right)^2 \tanh^2\left(\frac{e\psi}{4kT}\right) \quad (2)$$

where ρ_m and ρ_p are the medium and particle densities, κ is the Debye length, *a*, *b* and *c* are the particle semi-axes, and *g* is the gravitational acceleration constant. Within the particle-wall interaction, ε_m is the dielectric constant of the medium, ψ is the surface potential of the surface and particle, *T* is the absolute temperature, and *e* is the elementary electron charge. By then considering quasi-2D states at a fixed elevation and orientations relative to the substrate, the potential energy simplifies to,

$$u_i\left(x_i,\theta_i,\theta_j,r_{ij},\theta_{ij}\right) = u^{df}\left(x_i,\theta_i\right) + \sum_{j=1,j\neq i}^{N}u_{ij}^{pp}\left(x_i,\theta_i,\theta_j,r_{ij},\theta_{ij}\right) \quad (3)$$

where r_{ij} and θ_{ij} are the relative position and orientation of particle j with respect to particle i. The particle-particle potential is,

$$u_{ij}^{pp}\left(x_i,\theta_i,\theta_j,r_{ij},\theta_{ij}\right)=u_{ij}^{dd}\left(x_i,\theta_i,\theta_j,r_{ij},\theta_{ij}\right)+u_{ij}^{hp}\left(r_{ij},\theta_{ij}\right) \tag{4}$$

where u^{dd} is the dipole-dipole potential, and the hard wall repulsion between particles, u^{hp}, which is determined from the overlap condition for a given particle shape plus a small additive increase, δa. This increase accounts for electrostatic interactions, as given by a perturbation theory as,[32, 33]

$$\delta a=(1/2)\int_{2a}^{\infty}\left[1-\exp\left(-u_{ij}^e\left(r_{ij}\right)/kT\right)\right]dr_{ij} \tag{5}$$

which can be estimated using the electrostatic potential for spheres with thin double layers as,[34]

$$u_{ij}^e\left(r_{ij}\right)=B_{ij}^{pp}\exp\left[-\kappa\left(r_{ij}-2a\right)\right],\ B_{ij}^{pp}=32\pi\varepsilon_m a\left(\frac{kT}{e}\right)^2\tanh^2\left(\frac{e\psi}{4kT}\right) \tag{6}$$

where r_{ij} is the center-to-center distance of the two particles.

Dipole-Field Potential

The potential energy of a uniform dielectric particle in a high frequency electric field is,[28]

$$u=-\frac{1}{2}\mathbf{p}\cdot\mathbf{E} \tag{7}$$

where $\mathbf{E}$ is the interacting electric field, and $\mathbf{p}$ is the dipole moment. Analytical dipole moment expressions are limited to select particle geometries where the Laplace equation can be solved via separation of variables and for uniform polarization fields inside particle geometries with a second-degree surface. The dipole moment, $\mathbf{p}$, is,[28]

$$\mathbf{p}(x,\theta)=v_p\boldsymbol{\alpha}\cdot\left[\mathbf{A}_T(\theta)\cdot\mathbf{E}(x)\right] \tag{8}$$

where v_p is particle volume, $\boldsymbol{\alpha}$ is effective polarizability, $\mathbf{E}$ is the applied electric field in lab coordinates, and $\mathbf{A}_T$ is the rotation transformation matrix for angle θ. For a dielectric sphere, the particle volume is,

$$v_{p,s}=(4/3)\pi a^3 \tag{9}$$

and polarization is equal for each axis to give a scalar value of,

$$\alpha=3\varepsilon_m\left(\frac{\tilde{\varepsilon}_p-\tilde{\varepsilon}_m}{\tilde{\varepsilon}_p+2\tilde{\varepsilon}_m}\right)=3\varepsilon_m f_{cm} \tag{10}$$

where subscripts p and m denote particle and medium complex permittivities $\tilde{\varepsilon}$ given as,

$$\tilde{\varepsilon}_m=\varepsilon_m-\sqrt{-1}\frac{\sigma_m}{\omega},\ \tilde{\varepsilon}_{p,r_A}=\varepsilon_p-\sqrt{-1}\frac{\sigma_{p,r_A}}{\omega}. \tag{11}$$

Where ω is frequency, f_{cm} is the Clausius-Mossotti factor, and σ is conductivity for each primary axis r_A of the particle. The net dipole-field potential energy of a dielectric sphere is then,[30]

$$u^{df}\left(x_i\right) = -\frac{3}{2}v_p\varepsilon_m f_{cm}E_f\left(x_i\right)^2. \tag{12}$$

For an ellipsoid with semi-axes a, b, and c, the particle volume is,

$$v_{p,e} = \left(4/3\right)\pi abc \tag{13}$$

and the polarization for each principal axis $A=(x_A,\ y_A,\ z_A)$ for particle i is,[28]

$$\alpha_{el,AA} = 3\varepsilon_m\left(\frac{\varepsilon_{p,r_A} - \varepsilon_m}{3((\varepsilon_{p,r_A} - \varepsilon_m)L_{r_A}\left(\infty\right) + \varepsilon_m)}\right) = 3\varepsilon_m f_{cm,AA} \tag{14}$$

which simplifies to the result in Eq. (10) when $a = b = c$. Here, the depolarization factor, L_{r_A}, is,

$$L_{r_A}\left(\infty\right) = 0.5\varepsilon_0 abc\int_0^\infty (s+r_A^2)^{-1}\left[(s+a^2)(s+b^2)(s+c^2)\right]^{-0.5}ds \tag{15}$$

Using Eq. (7), the net dipole-field potential of a tri-axial dielectric ellipsoid is,[9]

$$u_i^{df}(x_i,\theta_i) = -\frac{3}{2}v_p\varepsilon_m\mathbf{f}_{cm}\cdot\left[\mathbf{A}_T(\theta_i)\cdot\mathbf{E}_f(x_i)\right] \tag{16}$$

where θ_i is the angle between lab x-unit vector and the particle's principal axis applied using rotation matrix, $\mathbf{A}_T(\theta)$, as,[10]

$$\mathbf{A}_T(\theta) = \begin{pmatrix} A_{T,11} & A_{T,12} & A_{T,13} \\ A_{T,21} & A_{T,22} & A_{T,23} \\ A_{T,31} & A_{T,32} & A_{T,33} \end{pmatrix} = \begin{pmatrix} \cos\theta & \sin\theta & 0 \\ -\sin\theta & \cos\theta & 0 \\ 0 & 0 & 1 \end{pmatrix} \tag{17}$$

Dipole-Dipole Potential

The point dipole potential for two spheres i and j can also be derived using Eq. (7), where a polarizable particle is interacting with the external electric field generated by another particle. The electric field generated by a dielectric polarized particle is dependent on the strength of the polarizing field and the distance away from that particle. When the gradient of the electric field is much larger than the particle size, the dipole within the particle generates a local field defined as,[35]

$$\mathbf{E}_{ij}(x_i,r_{ij},\theta_{ij}) = -\nabla\phi_{ij}(x_i,r_{ij},\theta_{ij})$$
$$\mathbf{E}_{ij}(x_i,r_{ij},\theta_{ij}) = f_{cm}E_f(x_i)\left[\sin\theta_{ij}\hat{\theta}_{ij} + 2\cos\theta_{ij}\hat{r}_{ij}\right] \tag{18}$$

where θ_{ij} is the angle between centers relative to the field direction. Further applications of Eq. (7) and the spherical dipole moment in Eq. (8) results in the point dipole-dipole potential,[36]

$$u_{ij}^{dd}\left(x_i,r_{ij},\theta_{ij}\right) = C_s\left([3\cos^2\theta_{ij} - 1]\right)\left(2a/r_{ij}\right)^3 \tag{19}$$

$$C_s = -2v_p\varepsilon_m\left\langle f_{cm}\right\rangle^2\left|\mathbf{E}_f\right|^2 \tag{20}$$

where $\langle f_{cm}\rangle$ is the average Clausius-Mossotti factor of all axes. For anisotropic dielectric ellipsoids, the dipole-dipole potential for particle i and neighbor j is calculated for each axis using Eq. (7). Each component of the field generated, $\mathbf{E}_{ij}$, by each axis of polarized ellipsoid j at the location of

particle i, E_{ij}, as,

$$E_{ij,B} = 3\delta_{BC} f_{cm,BB} E_C (L_{r_C}(\xi) - L_{r_C}(\infty)) + 3 f_{cm,BB} E_C \left(x_C \frac{\partial L_{r_C}(\xi)}{\partial x_B} \right) \tag{21}$$

where B and C are the indexes along the main axes of particle j. The ellipsoidal coordinate ξ is solved using,

$$\frac{x_{ij}^2}{a^2 + \xi} + \frac{y_{ij}^2}{b^2 + \xi} = 1 \tag{22}$$

in particle j coordinate, which leads to the dipole-dipole potential on particle i caused by particle j as,

$$u_{ij}^{dd,e}\left(x_i, \theta_i, \theta_j, r_{ij}, \theta_{ij}\right) = -v_p \varepsilon_m \left[\mathbf{f}_{cm} \cdot \left(\mathbf{A}_T(\theta_i) \cdot \mathbf{E}_f \right) \right] \cdot \left[\mathbf{A}_T(\theta_i - \theta_j) \cdot \mathbf{E}_{ij} \right] \tag{23}$$

Coplanar Electrode Field

The electric field, $\mathbf{E}_f$ components in Eq. (8) for parallel thin-film coplanar electrodes of separation, d, is[37]

$$E_{f,x} = E_0 \left[\tan^{-1}\left(\frac{\sin \hat{x}}{\sinh \hat{z}} \right) - \tan^{-1}\left(\frac{\cos \hat{x}}{\sinh \hat{z}} \right) \right]$$

$$E_{f,z} = \frac{E_0}{2} \left[\ln \left(\frac{\cosh \hat{z} + \cos \hat{x}}{\cosh \hat{z} - \cos \hat{x}} \frac{\cosh \hat{z} + \sin \hat{x}}{\cosh \hat{z} - \sin \hat{x}} \right) \right] \tag{24}$$

$$\hat{x} = \pi(x+d)/2d + \pi/4, \quad \hat{z} = \pi z_m / 2d$$

where $E_0 = V_{pp}/(\pi d)$, V_{pp} is the peak-to-peak voltage, d is the electrode gap and $z_m = c + h_m$ is the most probable particle height using Eq. (2).

Materials & Methods

Particle Fabrication

Anisotropic epoxy particles were fabricated using photolithography. Omnicoat (MicroChem), was spin coated onto a silicon wafer to provide a sacrificial layer. On top of the Omnicoat, SU-8 2002 (MicroChem) was spin coated to the desired thickness. A photomask was used to pattern particles at an exposure energy of 80 mJ/cm². Particles were lifted off the substrate with Remover PG (MicroChem), which dissolved the Omnicoat layer. Particles were rinsed with isopropyl alcohol and dispersed in deionized water. The particle geometry (**Fig. 1a**) is a rectangular prism capped with ellipse ends with dimensions in **Table 1**. Particle surface charge was maximized by washing with sulfuric acid to favor stability against unwanted aggregation and deposition.[9, 38]

Electrode Cell

An o-ring (McMaster-Carr) was coated with high vacuum grease and placed on a cleaned, patterned interdigitated electrodes (300 μm electrode with a 97 μm gap). The electrodes were cleaned by sonication in isopropyl alcohol for 30 minutes, acetone for 30 minutes, isopropyl alcohol for 30 minutes, rinsing with DI water, immersing in Nochromix (Godax) for 15 minutes, rinsing again with DI water, then dried with nitrogen. The particle dispersion is placed inside the

o-ring, which was sealed with a cover slip to prevent evaporation. Wires were attached to the leads of the electrodes, which were then connected to a function generator (Agilent 33220A).

Microscopy & Image Analysis

Position and orientation of particles between parallel electrodes were measured using an inverted microscope (Zeiss) with a 40x objective (**Fig. 1c**). Videos were captured at 5 frames/s using a CCD camera (Hamamatsu, Orca-ER) and Streampix (Norpix) software. Particle positions (x, y) and orientations (θ) were obtained in stacks of 30,000 frames using a particle tracking algorithm in MATLAB. The tracking algorithm (as in previous work[31]), in brief, was based on the following steps: (1) Gaussian smoothing to remove noise, (2) thresholding to differentiate (dark) background and (bright) foreground pixels, which was used to generate a binary image, (3) locating connected high intensity regions using a convex Hull algorithm to capture particle shape, and (4) using the resulting pixel set to determine particle centroid coordinates and endpoints to yield the projected long-axis dimension and lab-frame angle (θ).

Table 1. Known parameters from experiments and previous studies used to in Eq. (3) to calculate two-dimensional potential energy landscapes in Fig. 2 and all MC simulations. Values obtained from: [a]optical microscopy, [b]thin film analyzer, [c]manufacturer values (MicroChem), [d]handbook values,[39] [e]conductivity meter, [f]previous experiments[9], [g]Eq. (2) and [h]Eq.(5).

Parameter	Value	Parameter	Value
a, b, c $(\mu m)^{,b}$	5.0, 1.3, 0.85	d $(\mu m)^a$	97
ρ_p (kg/m³)^c	1200	$\varepsilon_p/\varepsilon_0{}^c$	3.2
ρ_m (kg/m³)^d	1000	$\varepsilon_m/\varepsilon_0{}^d$	78.5
κ^{-1} (nm)^e	30	σ_m $(\mu S/cm)^e$	10
ψ (mV)^f	-50	$\sigma_{px}, \sigma_{py}, \sigma_{pz}$ $(\mu S/cm)^f$	50, 20, 20
h_m $(\mu m)^g$	0.25	δa $(\mu m)^h$	0.13

Monte Carlo Simulations

We consider a canonical (NVT) ensemble of particles with the size and shape of the fabricated particles using the potential in Eq. (3) and parameters listed in Table 1.[40] The particles are constrained in two dimensions with only rotation and translation in a plane parallel to the substrate (**Fig. 1b**). Simulations include ~70 hard particles with periodic boundary conditions in the direction parallel to the electrodes (**Fig. 1d**). Equilibrium distribution functions were obtained for 10^5 steps after equilibration starting from a rectangular lattice configuration. Hard-particle repulsion is based on the experimentally characterized shape (**Fig. 1a**), which is approximated as a rectangular prism with elliptical end caps as,

$$\left|y_m\left(x_m\right)\right| = \begin{cases} (b+\delta a)\left[1-\dfrac{\left(x_m-0.6a\right)^2}{\left(0.4a+\delta a\right)^2}\right]^{0.5} + \delta a & \left|x_m\right| > 0.6a \\ b+\delta a & \left|x_m\right| < 0.6a \end{cases} \tag{25}$$

Where y_m and x_m are the geometric particle boundary mesh. A refined mesh along the particle perimeter is used to evaluate the overlap condition in particle coordinates as,

$$u_{ij}^{hp} = \begin{cases} \infty & y_{m,j}\left(x_{m,j}\right) \le y_{m,i}\left(x_{m,i}\right) \\ 0 & y_{m,j}\left(x_{m,j}\right) > y_{m,i}\left(x_{m,i}\right) \end{cases} \tag{26}$$

For the rectangular prism with elliptical end caps, the particle volume is,

$$v_{p,rpe} = \left[(24/5) + \pi(4/5)\right]abc \tag{27}$$

Inverse Monte Carlo (iMC) Simulations

Inverse MC simulations are used in this work to determine an energy landscape, *u*, using iterative forward MC simulations that converge based on matching experimental and simulated density profiles (ρ_{exp} and ρ_{sim}). For each iteration *k*, the inverse MC algorithm compares density distributions between simulation and an experiment to provide a revised estimate for the energy landscape in the *k+1* iteration as,[21, 22, 41-44]

$$u_{k+1} = u_k + 0.5kT\left[\left(\rho_{sim,k}/\rho_{exp}\right)-1\right] \tag{28}$$

In our implementation in this work, we adapt this general algorithm to adjust theoretical dipole-dipole potentials by comparing angular pair distribution functions at the radial contact distance r_c as,

$$u_{k+1}^{dd}\left(r_c,\theta_{12}\right) = u_k^{dd}\left(r_c,\theta_{12}\right) + 0.5kT\left[\frac{\rho_{sim,k}\left(r_c,\theta_{12}\right)}{\rho_{exp}\left(r_c,\theta_{12}\right)}-1\right] \tag{29}$$

where the initial configuration of *k+1* is the final configuration of simulation *k*. For concentrated particles, the polarization of each particle depends on the local electric field due to the applied external field and surrounding particles with induced dipoles.[36, 45] The simplest way to account for such an effect is to consider a multiplicative scalar factor, $f_k(\eta)$, modifying the single particle ellipsoidal dipole-field (Eq. (16)) and dipole-dipole (Eq. (23)) potentials as,

$$u_k^{df}(x_i,\theta_i) = f_k(\eta)u^{df}(x_i,\theta_i) \tag{30}$$

$$u_k^{dd,e} = f_k(\eta)u_k^{dd,e}\left(x_i,\theta_i,\theta_j,r_{ij},\theta_{ij}\right) \tag{31}$$

where $f_k(\eta)$ is adjusted in the iMC stepper in Eq. (29). Since out of plane position and orientation changes are shown to be insignificant in our analysis, the dipole field potential is two dimensional (**Fig. 2a,e**). In contrast, the dipole-dipole potential is higher dimensional as the result of every particle coordinates relative to each other. As a result, we use the projected potential to compare with the projected pair distribution function in Eq. (29). To obtain the projected two-dimensional potential, we obtain the average probability as,

$$\left\langle p_{ij}^{dd,e}\left(r_{ij},\theta_{ij}\right)\right\rangle_{x_i,\theta_i,\theta_j} = \frac{\int_{x_{i,o}}^{x_{i,f}} \int_{\theta_{i,o}}^{\theta_{i,f}} \int_{\theta_{j,o}}^{\theta_{j,f}} \exp\left(u_{ij}^{dd,e}\left(x_i,\theta_i,\theta_j,r_{ij},\theta_{ij}\right)\right)d\theta_j d\theta_i dx_i}{\left(x_{i,f}-x_{i,o}\right)\left(\theta_{i,f}-\theta_{i,o}\right)\left(\theta_{j,f}-\theta_{j,o}\right)} \tag{32}$$

which is then inverted to obtain the projected potential as (for use in Eq. (29), **Fig. 2b,e**),

$$\left\langle u_{ij}^{dd,e}\left(r_{ij},\theta_{ij}\right)\right\rangle_{x_i,\theta_i,\theta_j} = -\ln\left[\frac{\left\langle p_{ij}^{dd,e}\left(r_{ij},\theta_{ij}\right)\right\rangle_{x_i,\theta_i,\theta_j}}{\max\left\langle p_{ij}^{dd,e}\left(r_{ij},\theta_{ij}\right)\right\rangle_{x_i,\theta_i,\theta_j}}\right] \tag{33}$$

In addition to considering a concentration dependent factor in our iMC solver, we also investigate
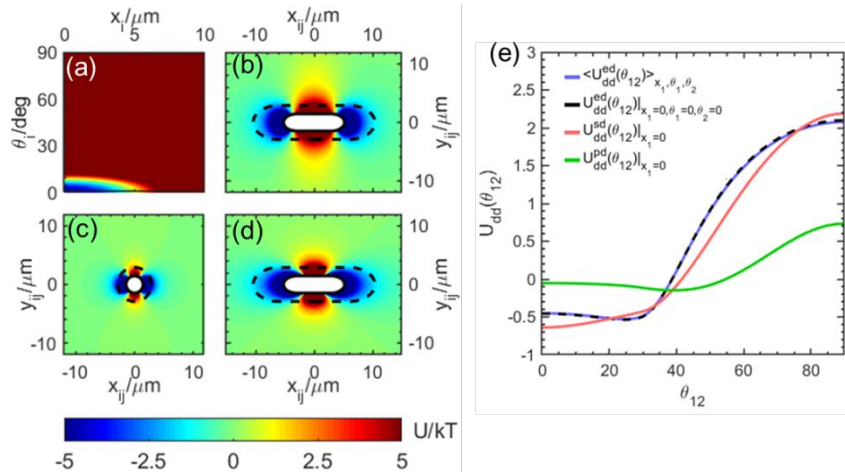
Fig. 2. Dipolar energy landscapes for anisotropic colloidal particles in AC electric fields. (a) Dipole-field potential for ellipsoidal particles in a 20V/mm, 5MHz AC electric field (Eq. (12)). (b) Ellipsoidal dipole-dipole potential (Eq. (23)) projected to two dimensions (Eqs. (32), (33)) using measured particle shape (Eq. (25)) and parameters in Table 1. (c) Point dipole-dipole potential (Eq. (19)) with same parameters as ellipsoidal point dipole except for single radius = *b*. (d) Stretched point dipole-dipole potential (Eq. (34)) from least squares fit to ellipsoidal dipole-dipole potential angular contact function. (e) Angular contact dependence for (green) point dipole-dipole potential, (blue) projected ellipsoidal dipole-dipole potential, (black) most probable dipole-dipole potential, and (red) best fit stretched point dipole-dipole potential.

stretching or compressing the usual point dipole potential (Eq. (19)) using,

$$u_k^{dd,s}\left(x_i, r_{ij}, \theta_{ij}, M_{x,k}, M_{y,k}\right) = f_k(\eta)C_s\left([3\cos^2\theta_T - 1]\right)\left(2/r_T\right)^3$$

$$r_T = \left[\left(M_{x,k}x_{ij}\right)^2 + \left(M_{y,k}y_{ij}\right)^2\right]^{0.5}, \quad \theta_T = \arctan\left(\frac{M_{y,k}y_{ij}}{M_{x,k}x_{ij}}\right) \tag{34}$$

where $M_{x,k}$ and $M_{y,k}$, stretch or compress the usual polar radial and angular dependence and C_s is defined in Eq. (20) (**Fig. 2 d,e**). In all cases, the iMC algorithm is initialized with $f_0(\eta)=1$ using the material properties and characterized quantities in Table 1. For the stretched point dipole case, initial values of $M_{x,0} = 0.405$ and $M_{y,0} = 0.812$ are obtained via a least squares fit of Eq. (34) to Eq. (23) using the angular contact dependence (**Fig. 2d**). The iMC stepper is considered to be converged when a desired tolerance, δ_k, is reached between the experimental and simulated density profiles given by,[41]

$$\delta_k = \left[\sum_{\theta_{ij}}\left(\rho_{\exp}\left(r_c, \theta_{ij}\right) - \rho_{\mathrm{sim},k}\left(r_c, \theta_{ij}\right)\right)^2\right]^{0.5} \tag{35}$$

Results & Discussion

Experimental Equilibrium Distributions

We performed experiments on microfabricated epoxy colloid particles sedimented onto a glass microscopy slide between parallel electrodes for observation with optical microscopy. We applied 5 MHz AC electric fields with different amplitudes including 4.1, 7.2, 10, 13, and 42 V/mm. Particles do not irreversibly deposit on the substrate or aggregate due to electrostatic repulsion. Particles are levitated above the substrate within a quasi-2D monolayer by a balance of electrostatic repulsion and gravity.[31] Particles sample 2D positions and orientations due to

Brownian motion which are tracked in real-time and then time averaged to produce equilibrium distribution functions. Finite thermal sampling of z, ϕ, and ψ for similar anisotropic particles was previously shown to produce no significant difference between projected and higher dimensional representations,[9] which is also the case in this work.

Fig. 3a shows representative images of particle configurations, and **Fig. 3b** shows particle center trajectories for 30 minutes. **Fig. 3c** shows time-averaged density profiles of particle centers relative to the electrode gap center. **Fig. 3d** shows the angular dependence of the particles' major axis relative to the electric field direction (*i.e.*, perpendicular to the parallel electrodes as seen in **Fig. 1b**). **Fig. 3e** shows the 2D pair distribution function for particle centers located in the vicinity of x=0 in the center of the electrode gap where the field is symmetric and most uniform.

For the field frequency used in this work, the preferred particle position and orientation is at electric field minimum parallel to the field direction. With increasing field amplitude, all data in **Fig. 3** show particles increasingly concentrate near the electrode center and align with the field direction. These observations are consistent with the dipole-field potential (Eq. (16), **Fig. 2a**) and
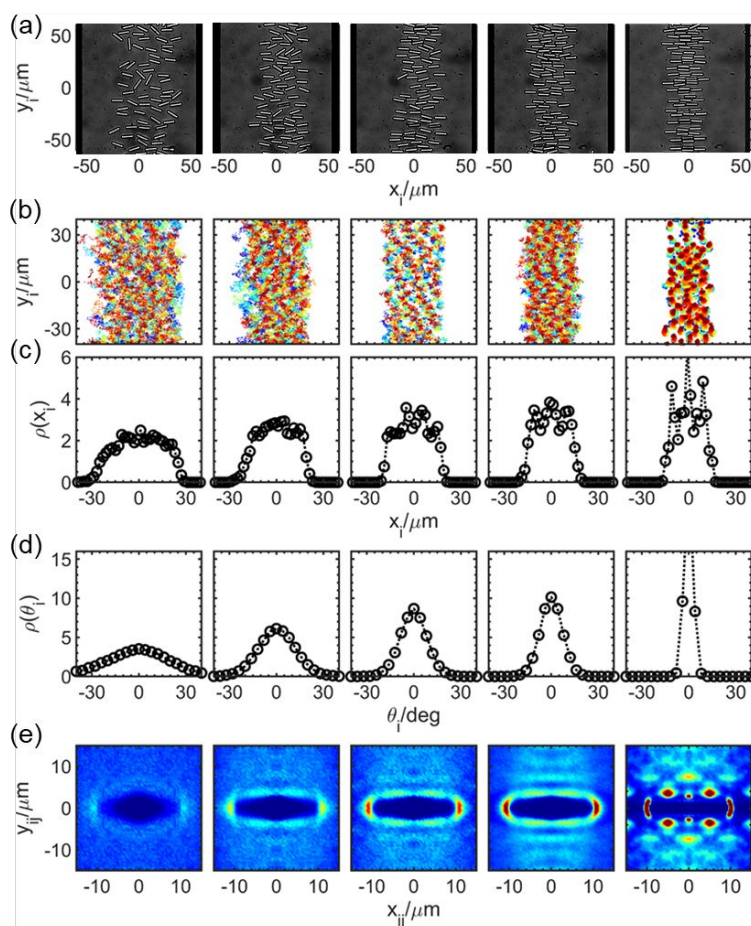
Fig. 3. Epoxy colloidal particle microstructures in nonuniform AC electric fields between coplanar parallel electrodes. AC electric field is 5 MHz and (left to right) 4.1, 7.2, 10, 13, and 42 V/mm. (a) Representative optical microscopy images of equilibrium particle configurations. (b) Particle center trajectories from t = 0 min (red) to t = 30 min (blue). (c) Particle position distribution relative to electrode gap center. (d) Particle orientation distribution relative to field direction. (e) Pair distribution function for particles in vicinity of electrode center ($|x_i|$<5μm) with 8-bit color scale for $\rho/<\rho>$=0 (blue) to 40 (red).

previous direct single particle measurements and models of anisotropic particles in AC electric fields.[9, 10] It is not known whether increasing particle concentration changes the infinitely dilute single particle dipole-field potential and how particle packing together with dipole-dipole potentials lead to the observed amplitude dependent configurations in Fig. 3. In the following we implement a novel inverse Monte Carlo (iMC) scheme to determine these interactions as a function of concentration and field amplitude.

Concentration Dependent Ellipsoidal Dipolar Potentials

Fig. 4 shows results from iMC simulations based on a concentration dependent correction, $f(\eta)$, to the dipole-field and dipole-dipole potentials for ellipsoids (Eqs. (30), (31)). All other parameters in the model potentials are fixed to the values reported in **Table 1** based on independent characterization and prior measurements.[9] **Fig. 4a** shows converged simulation renderings for comparison with experimental images in **Fig. 3a**. **Figs. 4b-d** show distribution functions from experiments (Fig. 3) compared to the initial and converged iMC simulation results using the concentration corrected ellipsoidal dipole potentials. The converged values of $f(\eta)$ are reported in **Fig. 6** for discussion in a final analysis after consideration of additional corrections. **Fig. 4e** shows the angular dependence in the first coordination shell of the pair distributions functions and free energy landscapes from experiments and simulations.

For all field amplitudes investigated in **Fig. 4**, the concentration corrected dipolar potentials improve agreement with measured distribution functions compared to potentials without $f(\eta)$. All values of $f(\eta)<1$ and monotonically decrease with increasing particle concentration, which is consistent with prior observations for spherical colloids in non-uniform AC electric fields.[21, 22, 30] Values less than unity indicate weaker dipole-field interactions, which results in sampling of a broader range of positions and orientations in lab coordinates (**Figs. 4b,c**). The pair distribution functions show less structure with values of $f(\eta)<1$, which is consistent weaker dipole-dipole interactions including both less dipolar repulsion along particle long axes in the field direction and less dipolar repulsion in perpendicular to the field direction.

The converged iMC simulation results based on concentration dependent potentials show good qualitative agreement with experiments at all field strengths and excellent quantitative agreement at lower fields. These results show that, once concentration effects and the hard core particle repulsion are taken into account, to first order, the dipole-field and dipole-dipole potentials for ellipsoids capture the behavior of liquid states well for the anisotropic particles. In more detail, although the anisotropic particles in this work deviate from ellipsoidal shapes, the ellipsoid potentials based on using the same major and minor axis dimensions work well for capturing liquid behavior using the concentration correction determined in **Fig. 4**. The concentration dependence is not surprising since it is predicted for spherical particles[36, 45] and has been measured and shown to be important for their quasi-2d phase behavior in nonuniform fields.[21, 22, 30]

Deviations between the experimental and simulated pair distribution functions become more pronounced at higher fields as particles become more concentrated and ordered. At higher fields, stronger dipolar potentials and stronger confinement of particles at the field minimum are both simultaneously important, so accurate dipole-dipole and dipole-field potentials are necessary to capture both effects. Given the discrepancies in the pair distribution functions at the highest fields where ordered states are observed, it appears additional effects need to be considered beyond the concentration dependence of dipolar interactions.
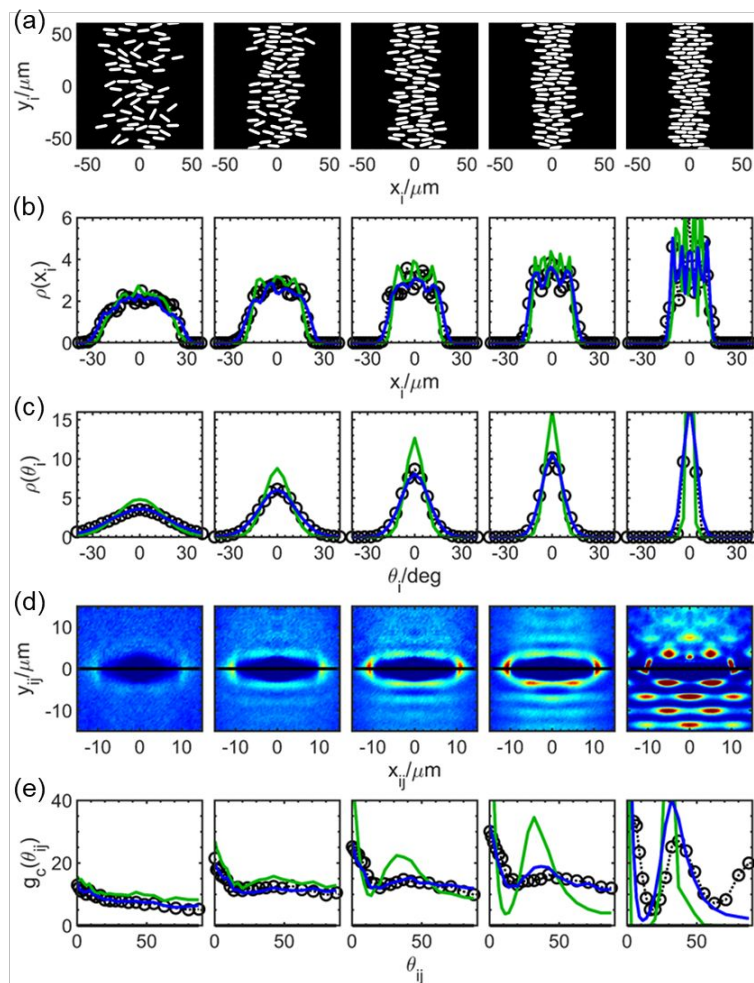
Fig. 4*. Comparison of experiments and iMC simulations using concentration dependent dipolar potentials. Plots show experiments (circles) vs. iMC simulation results for ellipsoidal point dipole (Eqs. (30),(31)) without (green) and with (blue) concentration dependent factor, $f(\eta)$, for field conditions in Fig. 3. (a) Representative converged simulation renderings. (b) Particle position distribution relative to electrode gap center. (c) Particle orientation distribution relative to field direction. (d) Pair distribution for particles in vicinity of electrode center ($|x_i|<5$ μm) with 8-bit color scale for $\rho/<\rho>=0$ (blue) to 40 (red) with (top) and without (bottom) $f(\eta)$. (e) First coordination shell pair distribution.

Stretched Point Dipolar Potentials

The functional form of the ellipsoidal point dipole (Eqs. (16), (23)) does not well capture the angular dependence of first coordination shell for particles in high fields, high concentrations, and ordered configurations, which occur simultaneously. It is not obvious how to modify the ellipsoid potential to perturb it in a manner that captures the additional functional dependence needed to match simulations to the measured pair distribution functions. An alternative anisotropic potential that we investigated, which retains some first principles concepts, as well as a relatively simple analytical form, is a point dipole potential stretched both parallel and perpendicular to the average direction of the particle long axis. By allowing a concentration dependence, and stretching in two directions, for a total of three adjustable parameters, we show in the following how such a potential optimized in an iMC scheme quantitatively captures all the experimental observations at different field amplitudes.

The results of converged iMC simulations based on stretch point dipoles are reported in Fig. 5. Experiments show excellent agreement with the rendered simulation configurations (**Fig. 5a**) and position and orientation distributions (**Figs. 5b,c**) for all fields and concentration profiles. In more detail, the position and orientation distributions for both the converged ellipsoid and stretched dipole potentials agree with experiments for all fields. This result is to be expected since the same dipole-field potential is used for both simulations that have different dipole-dipole potentials, which is shown to be accurate in **Fig. 4**. We refit the concentration dependent factor in the dipole-field potential in the iMC results when optimizing the new stretched point dipole-dipole potential, but it ultimately changed very little.

The pair distribution function (**Figs. 5d,e**) more directly correlates with the dipole-dipole contribution to the net pair potential, and therefore provides a more direct test of the optimal functional form. While both the ellipsoidal and stretched dipole-dipole perform equally well at low
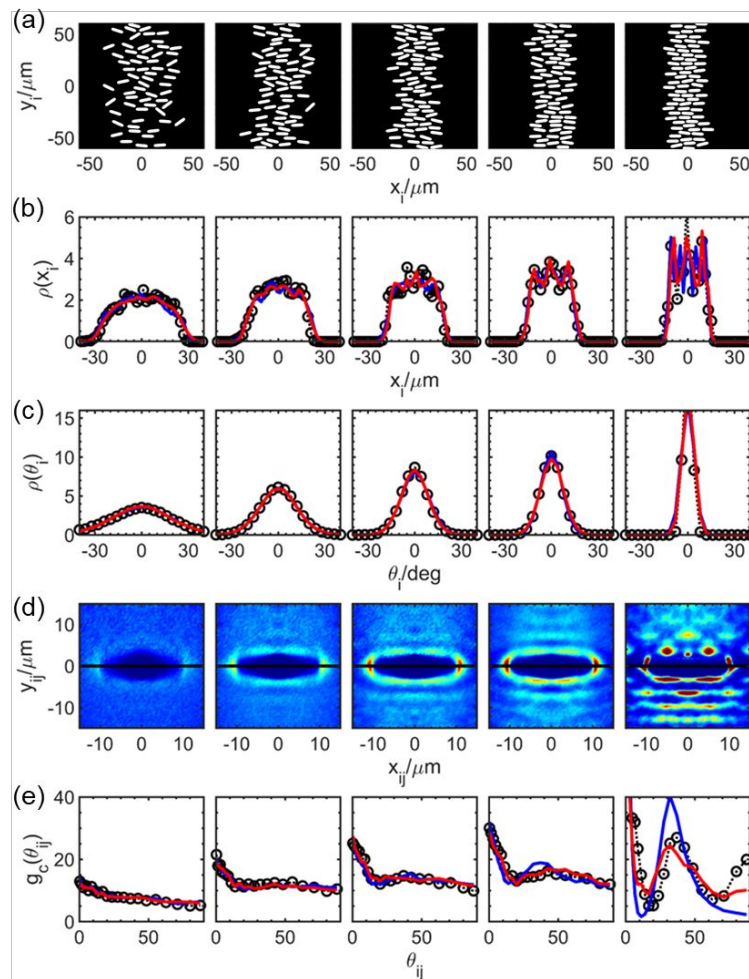
Fig. 5. Comparison of experiments and iMC simulations using stretched point dipolar potentials. Plots show experiments (circles) vs. iMC simulation results for (blue) ellipsoidal point dipole (Eqs. (31)) and (red) stretched point dipole (Eq. (34)), both with concentration dependent factor, $f(\eta)$, for field conditions in Fig. 3. (a) Representative converged simulation renderings. (b) Particle position distribution relative to electrode gap center. (c) Particle orientation distribution relative to field direction. (d) Pair distribution for particles in vicinity of electrode center ($|x_i|<5\mu m$) with 8-bit color scale for $\rho/<\rho>=0$ (blue) to 40 (red) with (top) and without (bottom) $f(\eta)$. (e) First coordination shell pair distribution.

fields in quasi-2D conditions, the stretched point dipole produces significantly better agreement with experiments at high fields. In particular, at the highest fields tested (13 and 42 V/mm), the stretched point dipole potential more accurately captures the full 2D pair distribution (**Fig. 5d**) and the angular contact distribution (**Fig. 5e**). While small quantitative differences persist in the magnitude of the density fluctuations in the crystal state, all other distribution functions are qualitatively and quantitatively captured for all fields tested. In addition, the small differences between simulations and experiments observed in the crystalline state at the highest field are also within the limits of uncertainty of the measurements. Practically, finite particle size polydispersity, shape non-uniformity, and spatial resolution limits (on particle positions and orientations) collectively produce some uncertainty in the experimental results and their comparison with models. Ultimately, the agreement between the simulation results based on the stretch point dipole and the experiments essentially agree in all cases within the limits of uncertainty of the measurements.

Analysis of Converged Potentials

The converged ellipsoidal pair potentials and adjustable parameters vs. field amplitude reveal several emergent features (**Fig. 6**). The projected two dimensional ellipsoidal energy landscapes (Eqs. (31), (34)) (**Fig. 6a**) show overall increasing amplitude with increasing field strength. While the concentration dependent prefactor, $f(\eta)$, decreases with increasing concentration associated with increasing field strength (**Fig. 6b**), the field dependent amplitude of the dipole potential still increases overall. The optimal ellipsoidal and stretched point dipoles are also shown to have nearly identical $f(\eta)$ dependences, showing this result is general for both dipole-dipole potentials. The decreasing value of $f(\eta)$ is expected based on the influence of concentrating dielectric particles on the local electric field,[36, 45] although the magnitude of the reduction for anisotropic particles is greater than prior measurements of spherical colloids (**Fig. 6b**).[21, 22, 30]

Like prior findings for spherical colloidal particles,[21, 22, 30] no dependence of potentials on particle configuration at a given concentration was detected for the anisotropic prism particles in this work. In short, a simple scalar correction based only on concentration (not configuration) consistently accounts for the magnitude of dipole-field and dipole-dipole potentials fit to all experiments in our iMC scheme. By considering experimentally determined $f(\eta)$ for spheres and the anisotropic particles in this work, the range of $f(\eta)$ appears to vary for shapes with aspect ratios from ~1-4. Because similar trends are observed for both aspect ratios, one could speculate that other convex particle shapes could be modeled using such a concentration dependent factor, which may depend on aspect ratio.

The optimized stretching parameters, M_x and M_y (**Fig. 6c**), show slightly increased magnitudes/ranges compared to the ellipsoidal point dipole (given the inverse relationship between M_x, M_y and magnitude, Eq. (34)). Attraction along the particle long axis shows a small monotonic increase with increasing particle concentration (and increasing field), whereas repulsion along the particle short axis shows a smaller decrease with increasing particle concentration (and increasing field). The differences in stretching attraction and repulsion along the particle major and minor axes yields potentials with different angular dependences and zero interaction occurring at different angles (**Fig. 6d**). The resulting change in the angular dependence of the contact pair potential most directly correlates with the field dependent changes in the contact pair distribution functions in **Figs. 3-5**. Although the change to the contact pair distribution function is most obvious in the crystalline state at the highest field, subtle changes to the potential and pair distribution function are also observed in concentrated liquid crystalline states.
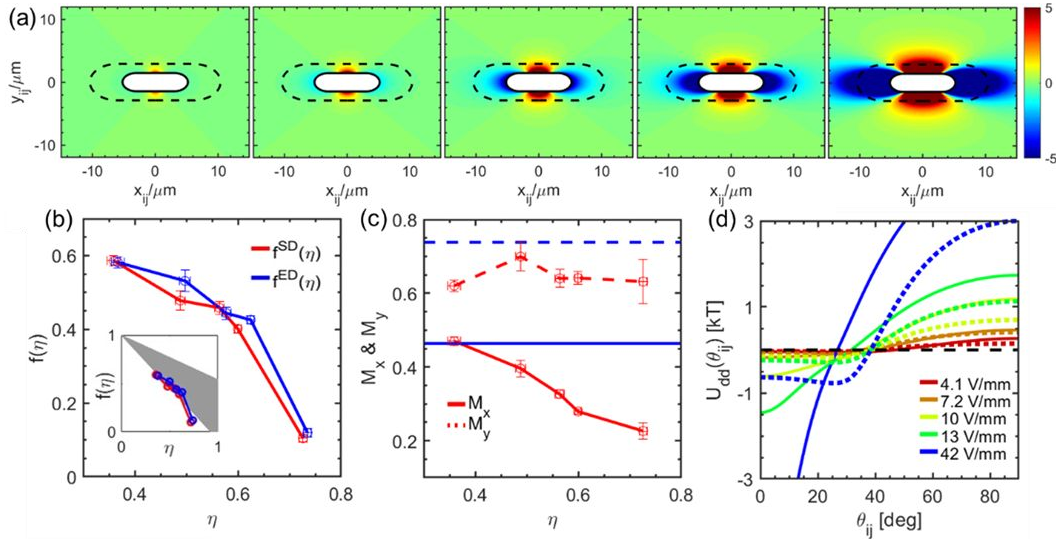
Fig. 6. Optimal net pair potentials and parameters from converged iMC simulations. (a) Net pair potentials, in units of kT, from superposition of hard core repulsion (dashed line) and stretched dipolar potentials (spectrum color scale) for orientation aligned with field for conditions in Fig. 3. Particle shape shown in white. (b) Concentration dependent prefactor, $f(\eta)$, for ellipsoid (blue) and stretched point (red) dipoles with (inset) grey region showing upper bound for aspect ratio 1 spheres[21] and lower bound for aspect ratio ~4 shapes in this work. (c) Dipole stretch factors for (blue) initial fit to ellipsoid potential and (red) after optimization via iMC fitting. Error bars indicate uncertainty between the experimental and converged simulated pair correlation functions. (d) Dipolar contact potential in first coordination shell for each voltage for (dashed) ellipsoidal dipole and (solid) stretched point dipole.

The resulting change in the angular dependence from the ellipsoidal point dipole model accounts for several complex phenomena that are to be expected for the non-ellipsoidal particle shape investigated in this work. The ellipsoid dipole model is calculated based on the electric field at the surface of a uniformly polarized ellipsoid,[28] which is obviously not the case for the particles in this work. Additionally, for a given center-to-center distance, the prism-like particles in our work have a larger contact region with more polarized material in closer proximity. We speculate that the stretched dipole model accommodates different edge and corner curvatures not accounted for by the ellipsoidal dipole and could therefore be adapted to other superellipse shapes intermediate between rhombuses, ellipses, and rectangles. Future investigations of systematically varying particle shapes could reveal trends for how stretched dipole parameters depend on geometric properties of different anisotropic particle shapes.

Finally, our models do not include the influence of neighboring dipoles on each particle's final induced dipole moment. Prior modeling work considering self-consistent dipole-dipole moments for both anisotropic particles and particles with corners has shown stronger interactions, particularly in end-to-end configurations.[26] The three parameters we introduce into our stretched point dipole model optimized via an iMC scheme effectively account for these effects. Future work on different particle shapes in AC electric fields could consider multipole potentials[46] as a route towards more accurate and general potentials, but our results for a single particle shape do not obviously require the additional analytical complexity. Additional investigation of other field conditions, multicomponent systems, and non-equilibrium conditions could reveal broader applicability of the simple analytical model in this work.

Conclusions

By quantitatively matching experimental and simulated configurations of anisotropic colloidal particles in high frequency AC electric fields, we identified analytical potentials for dipole-field and dipole-dipole interactions that accurately capture equilibrium microstructures. We tracked position and orientation of triaxial epoxy particles as a function of field amplitude to construct equilibrium distribution functions for non-uniform liquid and liquid crystal microstructures. We then implemented a novel inverse Monte Carlo simulation algorithm to determine optimal fits of analytical potentials for both dipole-field and dipole-dipole potentials. Our findings show that using an accurate particle volume and axis dimensions in an ellipsoidal dipole model along with a concentration dependent correction captures liquid and low density liquid crystals microstructures. To match experiments and simulations at all conditions including the highest fields, concentrations, and ordering, we developed a novel stretched point dipole potential form that provided the ability match the first coordination shell angular dependence in the pair distribution function. The analytical simplicity, accuracy, and adjustability of the stretched point dipole potential suggest it can be applied to model microstructures and assembly of systematically varying anisotropic particle shapes in AC electric fields in future work.

Acknowledgments

References

1. N. Wu, D. Lee and A. Striolo, *Anisotropic Particle Assemblies*, Elsevier, Amsterdam, 2018.
2. A. McDougal, B. Miller, M. Singh and M. Kolle, *Journal of Optics*, 2019, **21**, 073001.
3. J. Kim, J. Peretti, K. Lahlil, J.-P. Boilot and T. Gacoin, *Advanced Materials*, 2013, **25**, 3295-3300.
4. A. A. Shah, H. Kang, K. L. Kohlstedt, K. H. Ahn, S. C. Glotzer, C. W. Monroe and M. J. Solomon, *Small*, 2012, **8**, 1551-1562.
5. J. Yan, K. Chaudhary, S. Chul Bae, J. A. Lewis and S. Granick, *Nature Communications*, 2013, **4**, 1516.
6. R. R. Collino, T. R. Ray, R. C. Fleming, C. H. Sasaki, H. Haj-Hariri and M. R. Begley, *Extreme Mechanics Letters*, 2015, **5**, 37-46.
7. M. Cavallaro, L. Botto, E. P. Lewandowski, M. Wang and K. J. Stebe, *Proceedings of the National Academy of Sciences*, 2011, **108**, 20923-20928.
8. T. D. Edwards and M. A. Bevan, *Langmuir*, 2014, **30**, 10793-10803.
9. B. Rupp, I. Torres-Diaz, X. Hua and M. A. Bevan, *Langmuir*, 2018, **34**, 2497-2504.
10. I. Torres-Díaz, B. Rupp, Y. Yang and M. A. Bevan, *Soft Matter*, 2018, **14**, 934-944.
11. M. M. Panczyk, J. G. Park, N. J. Wagner and E. M. Furst, *Langmuir*, 2013, **29**, 75-81.
12. F. Dong, M. Liu, V. Grebe, M. D. Ward and M. Weck, *Chemistry of Materials*, 2020, **32**, 6898-6905.
13. I. Dozov, E. Paineau, P. Davidson, K. Antonova, C. Baravian, I. Bihannic and L. J. Michot, *J Phys Chem B*, 2011, **115**, 7751-7765.
14. A. C. Stelson, S. J. Penterman and C. M. Liddell Watson, *Journal of Materials Chemistry C*, 2018, **6**, 11118-11127.
15. B. Liu, T. H. Besseling, M. Hermes, A. F. Demirors, A. Imhof and A. van Blaaderen, *Nat Commun*, 2014, **5**, 3092.

16. A. Kuijk, T. Troppenz, L. Filion, A. Imhof, R. van Roij, M. Dijkstra and A. van Blaaderen, *Soft Matter*, 2014, **10**, 6249-6255.
17. K. Chaudhary, J. J. Juarez, Q. Chen, S. Granick and J. A. Lewis, *Soft Matter*, 2014, **10**, 1320-1324.
18. C. W. t. Shields, S. Zhu, Y. Yang, B. Bharti, J. Liu, B. B. Yellen, O. D. Velev and G. P. Lopez, *Soft Matter*, 2013, **9**, 9219-9229.
19. N. R. Famularo, R. S. Hendley, S. J. Boehm, X. Guo, T. S. Mayer, M. A. Bevan and C. D. Keating, *The Journal of Physical Chemistry C*, 2020, **124**, 18755-18769.
20. A. Yethiraj and A. v. Blaaderen, *Nature*, 2003, **421**, 513-517.
21. J. J. Juarez and M. A. Bevan, *J. Chem. Phys.*, 2009, **131**, 134704.
22. J. J. Juarez, B. G. Liu, J.-Q. Cui and M. A. Bevan, *Langmuir*, 2011, **27**, 9219-9226.
23. A. Kuijk, T. Troppenz, L. Filion, A. Imhof, R. van Roij, M. Dijkstra and A. van Blaaderen, *Soft Matter*, 2014, **10**, 6249-6255.
24. J. J. Crassous, A. M. Mihut, E. Wernersson, P. Pfleiderer, J. Vermant, P. Linse and P. Schurtenberger, *Nature Communications*, 2014, **5**, 5516.
25. A. A. Shah, B. Schultz, W. Zhang, S. C. Glotzer and M. J. Solomon, *Nat Mater*, 2015, **14**, 117-124.
26. B. W. Kwaadgras, R. van Roij and M. Dijkstra, *The Journal of Chemical Physics*, 2014, **140**, 154901.
27. T. Troppenz, A. Kuijk, A. Imhof, A. van Blaaderen, M. Dijkstra and R. van Roij, *Phys Chem Chem Phys*, 2015, **17**, 22423-22430.
28. J. A. Stratton, *Electromagnetic Theory*, McGraw-Hill Book Company, Inc., New York, 1941.
29. J. P. Singh, P. P. Lele, F. Nettesheim, N. J. Wagner and E. M. Furst, *Physical Review E*, 2009, **79**, 050401.
30. J. J. Juarez, J.-Q. Cui, B. G. Liu and M. A. Bevan, *Langmuir*, 2011, **27**, 9211-9218.
31. J. L. Bitter, Y. Yang, G. Duncan, H. Fairbrother and M. A. Bevan, *Langmuir*, 2017, **33**, 9034-9042.
32. J. A. Barker and D. Henderson, *J. Chem. Phys.*, 1967, **47**, 4714-4721.
33. J. Zhang, Y. Zhang and M. A. Bevan, *J Chem Phys*, 2020, **152**, 054905.
34. W. B. Russel, D. A. Saville and W. R. Schowalter, *Colloidal Dispersions*, Cambridge University Press, New York, 1989.
35. H. Morgan and N. G. Green, *AC Electrokinetics: Colloids and Nanoparticles*, Research Studies Press, 2003.
36. P. M. Adriani and A. P. Gast, *Phys. Fluids*, 1988, **31**, 2757-2768.
37. H. Morgan, A. García Izquierdo, D. Bakewell, N. G. Green and A. Ramos, *Journal of Physics D: Applied Physics*, 2001, **34**, 1553-1561.
38. S. L. Tao, K. Popat and T. A. Desai, *Nat Protoc*, 2006, **1**, 3153-3158.
39. D. R. Lide, ed., *CRC Handbook of Chemistry and Physics*, CRC Press, New York, 2000.
40. M. P. Allen and D. J. Tildesley, 2017.
41. A. K. Soper, *Chemical Physics*, 1996, **202**, 295-306.
42. H.-J. Wu, T. O. Pangburn, R. E. Beckham and M. A. Bevan, *Langmuir*, 2005, **21**, 9879-9888.
43. T. O. Pangburn and M. A. Bevan, *J. Chem. Phys.*, 2006, **124**, 054712.
44. T. O. Pangburn and M. A. Bevan, *J. Chem. Phys.*, 2005, **123**, 174904.
45. R. Tao and J. M. Sun, *Phys. Rev. Lett.*, 1991, **67**, 398.

46. T. B. Jones and M. Washizu, *J. Electrostatics*, 1994, **33**, 199-212.